STRUCTURAL BIOLOGY

Histone modification–driven structural remodeling unleashes DNMT3B in DNA methylation

Chao-Cheng Cho[1], Hsun-Ho Huang[1,2], Bo-Chen Jiang[1], Wei-Zen Yang[1], Yi-Ning Chen[1], Hanna S. Yuan[1,2]*

The DNA methyltransferase 3B (DNMT3B) plays a vital role in shaping DNA methylation patterns during mammalian development. DNMT3B is intricately regulated by histone H3 modifications, yet the dynamic interplay between DNMT3B and histone modifications remains enigmatic. Here, we demonstrate that the PWWP (proline-tryptophan-tryptophan-proline) domain within DNMT3B exhibits remarkable dynamics that enhances the enzyme's methyltransferase activity upon interactions with a modified histone H3 peptide (H3K4^{me0}K36^{me3}). In the presence of H3K4^{me0}K36^{me3}, both the PWWP and ADD (ATRX-DNMT3-DNMT3L) domains transition from autoinhibitory to active conformations. In this active state, the PWWP domain most often aligns closely with the catalytic domain, allowing for simultaneous interactions with H3 and DNA to stimulate DNA methylation. The prostate cancer–associated DNMT3B R545C mutant is even more dynamic and susceptible to adopting the active conformation, resulting in aberrant DNA hypermethylation. Our study suggests the mechanism by which conformational rearrangements in DNMT3B are triggered by histone modifications, ultimately unleashing its activity in DNA methylation.

INTRODUCTION

Epigenetic modifications encompass a range of molecular processes, including histone modifications and DNA methylation. These modifications constitute heritable changes in gene expression patterns, influencing the behavior of specific genomic loci or chromosomes while leaving the underlying DNA sequence unchanged (*1*). In mammals, DNA methylation occurs exclusively at cytosine residues, predominately at CpG sites, by a trio of DNA methyltransferases (DNMTs): DNMT1 (DNA methyltransferase 1), DNMT3A, and DNMT3B (*2*, *3*). Within the human genome, there are ~28 million CpG sites, with 60 to 80% exhibiting methylation, which are commonly associated with transcriptional silencing of retrotransposons, imprinted genes, and the X chromosome in female cells, as well as selective exposure of gene promoters to transcription factors. The methylation activities of DNMTs are subject to an array of regulatory controls, orchestrated by chromatin modifications, chromatin-associated proteins, chromatin remodeling enzymes, and environ mental cues (*4*, *5*). Understanding the mechanisms governing the recruitment of DNMTs to chromosomes for methylation of their targets, such as the interplay between chromatin modifications and DNA methylation, is of profound significance in deciphering the intricacies of epigenetic gene regulation.

All members of the DNMT family of enzymes in mammals share a common C-terminal catalytic methyltransferase domain (CD), which catalyzes the transfer of a methyl group from the cofactor *S*-adenosyl methionine to cytosines within DNA. In mammalian development, the de novo methyltransferases DNMT3A and DNMT3B play a crucial role in establishing DNA methylation patterns during embryogenesis (*6*). Notably, these two enzymes share a similar domain organization, characterized by the presence of a PWWP (proline-tryptophan-tryptophan-proline) domain and an ADD (ATRX-DN MT3-DNMT3L) domain, followed by a CD (Fig. 1). Within the DNMT3 family, DNMT3L is distinctive in having a truncated DNA methyltransferase-like domain (CLD), rendering it devoid of methyltransferase activity. However, DNMT3L plays a unique role in protein complex formation, interacting with DNMT3A and DNMT3B and allosterically enhancing their methyltransferase activities (*7*–*10*).

Crystal structures of the CD of DNMT3A in complex with the CLD of DNMT3L (referred to as the DNMT3A-3L complex), as well as the DNMT3B-3L complex, have revealed a tetrameric linear CLD-CD-CD-CLD arrangement, with the DNA snugly bound within the core CD-CD of dimeric DNMT3A and DNMT3B (*11*–*14*). DNMT3A and DNMT3B use two flexible loops to clamp the DNA strand, with their target recognition domain loops bound at the major groove, while the catalytic loop is bound at the minor groove, adeptly flipping out the cytosine base for methylation. The N-terminal ADD domain within DNMT3A specifically recognizes the unmethylated K4 in the histone H3 tail (H3K4^{me0}), and DNMT3A activity is repressed by H3K4 methylation (*15*). The PWWP domain within DNMT3A reads trimethylated K36 in the H3 tail (H3K36^{me3}) to guide DNMT3A to chromatin (*16*). Paralleling this scenario, methylation of K36 in H3 by the methyltransferase SETD2 and the presence of the PWWP domain within DNMT3B jointly act as essential components for methylation of actively transcribed genes by DNMT3B (*17*).

The ADD domain in the DNMT3 family of enzymes contains a PHD-finger motif, which is one of the chromatin-binding modules for readout of modified or unmodified lysine marks in histones (*18*). A crystal structure of the ADD domain of DNMT3L revealed that this PHD-finger motif embedded in the cysteine-rich ADD domain bears acidic residues for interactions with unmodified K4 (H3K4^{me0}) (*19*). Crystal structures of a truncated DNMT3A construct containing the ADD domain and CD have further indicated that the ADD domain blocks the CD responsible for DNA binding, thereby autoinhibiting the enzyme's methyltransferase activity (*20*). Upon binding of an ADD domain to a histone H3 tail peptide harboring an unmethylated K4 (H3K4^{me0}), the ADD domain undergoes a conformational rearrangement that releases DNMT3A from autoinhibition (*20*).

[1]Institute of Molecular Biology, Academia Sinica, Taipei, Taiwan 11529, ROC. [2]Graduate Institute of Biochemistry and Molecular Biology, National Taiwan University, Taipei, Taiwan 10048, ROC.
*Corresponding author. Email: hanna@sinica.edu.tw

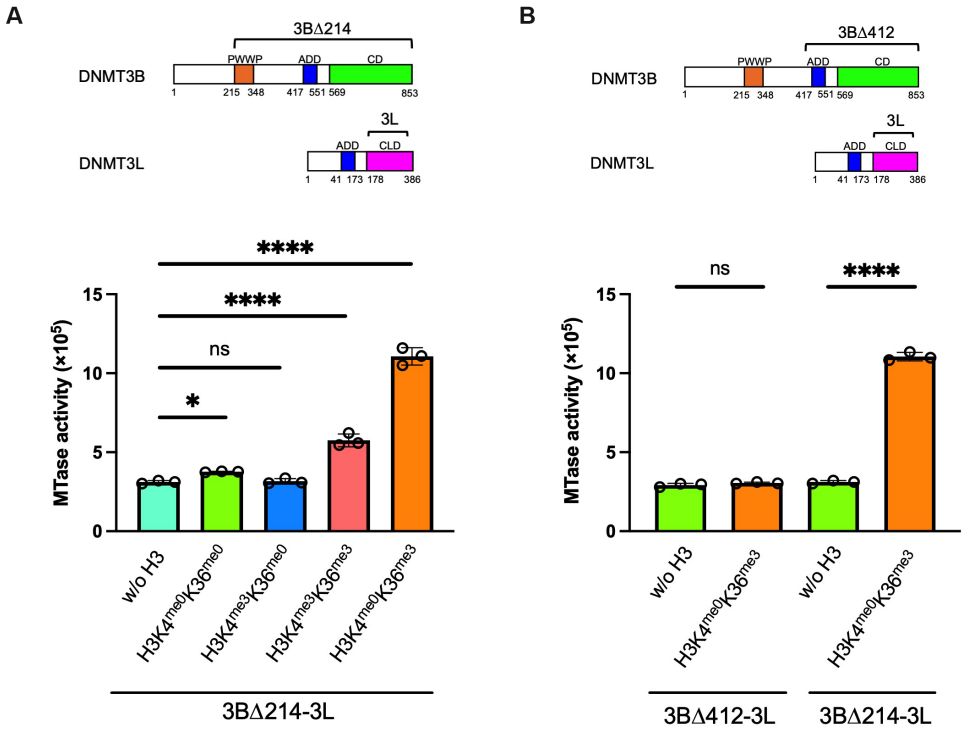

Fig. 1. The PWWP domain within DNMT3B is required for the histone H3 peptide–mediated stimulation of the methyltransferase activity of the DNMT3B-3L complex. (**A**) Methyltransferase activities of 3BΔ214-3L in the absence or presence of the H3 tail peptide with methylated and/or unmethylated K4 and K36 were measured using MTase-Glo assays by three independent experiments. The 40–amino acid H3K4^{me0}K36^{me3} peptide (residues 1 to 40) most strongly stimulated the methyltransferase activity of 3BΔ214-3L in methylating 40-bp DNA. MTase, methyltransferase. (**B**) The H3K4^{me0}K36^{me3} peptide did not enhance the methyltransferase activity of 3BΔ412-3L, but it did increase the activity of 3BΔ214-3L. The average of three independent experiments is shown with error bars representing 1 SD. Statistical significance (*P* values) was determined by two-tailed Student's *t* test: *$P < 0.1$ and ****$P < 0.0001$; ns, not significant.

The PWWP domain belongs to the Royal superfamily of modules that are involved in recognizing dimethylated or trimethylated lysines in histones (*21*). More than 20 PWWP domain–containing proteins have been identified in the human genome, and they are usually involved in chromatin-associated processes and bind both histones and DNA. A crystal structure of the PWWP domain of mouse Dnmt3b revealed a barrel-like fold packed with a helix bundle structure, which exhibits a basic surface patch presumably involved in nonspecific DNA binding (*22*). The crystal structure of the PWWP domain of human DNMT3B bound with a 12–amino acid H3K36^{me3} peptide further showed that a trimethylated lysine is inserted into an aromatic cage in a way similar to the Royal superfamily domains known to bind methylated histones (*23*). The cryo–electron microscopy (cryo-EM) structure of a DNMT3A2-DNMT3B3 complex bound with a mononucleosome core particle unveiled that the CD of DNMT3A2 binds to extranucleosomal DNA of the nucleosome, whereas the inactive CLD of DNMTB3 binds to the nucleosome core, thereby providing the structural basis for the enzyme's preferential methylation of chromosomes at linker regions (*24*). The cryo-EM structures of DNMT3B homo-oligomers have further revealed that the ADD domain may assemble with the CD in an autoinhibitory conformation, reminiscent of DNMT3A autoinhibition reported previously (*25*). However, the PWWP domains in these DNMT3B oligomers mostly remain undetectable, indicating a remarkable degree of conformational flexibility. Therefore, while structural investigations have unveiled various modes of H3 peptide binding to the ADD and PWWP domains, as well as the CD's interactions with the ADD domain, DNA, or nucleosomes, the precise molecular mechanism of how histone modifications regulate DNMT3's activity via the PWWP and ADD domains has remained elusive.

In this study, combining various biochemical and biophysical techniques, we investigated the intricate interplay among human DNMT3B, H3 peptides, and DNA to provide the molecular basis for how H3 histone modifications regulate DNA methylation. We show that the PWWP domain in DNMT3B strongly enhances the activity of the DNMT3B-3L complex through interactions with the modified histone H3 peptide with a trimethylated K36. We resolved a crystal structure of the PWWP domain and, together with biochemical data, show that the PWWP domain is involved in DNA binding in the presence of the H3 peptide. Using small-angle x-ray scattering (SAXS), we further show that both the ADD and PWWP domains are rearranged in DNMT3B from an autoinhibitory to active conformation in the presence of the modified histone H3 peptide (H3K4^{me0}K36^{me3}). Notably, in the active conformation, the PWWP domain undergoes a substantial shift, aligning itself adjacent to the CD in a position appropriate for DNA binding. This structural rearrangement plays a crucial role in augmenting stable assembly of the epigenetic DNMT3B-3L-H3-DNA complex. We also show by SAXS and molecular dynamics simulations that a prostate cancer–related DNMT3B R545C mutant, which displays hypermethylation activity, becomes even more flexible than a wild-type enzyme in adopting the active conformation through interactions with the modified histone

H3 tail. Thus, our findings illuminate the intricate molecular mechanism responsible for stimulating DNMT3B activity through structural remodeling by histone modifications.

RESULTS

The PWWP domain profoundly enhances the activity of DNMT3B through interactions with the H3K4^{me0}K36^{me3} peptide

To investigate the regulatory mechanism of human DNMT3B, we expressed various N-terminally truncated variants of DNMT3B in *Escherichia coli*, including 3BΔ214 (residues 215 to 853, containing the PWWP, ADD, and CD), 3BΔ412 (residues 413 to 853, containing the ADD and CD), and the PWWP domain alone (residues 226 to 355) (Fig. 1). Both recombinant 3BΔ214 and 3BΔ412 lacking the N-terminally disordered region were soluble and stable, so they could be copurified with the CLD of DNMT3L (residues 179 to 379) as tetrameric 3BΔ214-3L and 3BΔ412-3L complexes. All of our protein samples, including 3BΔ214-3L, 3BΔ412-3L, and PWWP, were purified to high homogeneity, as shown by gel filtration profiles and SDS–polyacrylamide gel electrophoresis (fig. S1).

Next, we assessed the methyltransferase activity of the DNMT3B-3L complexes by means of MTase-Glo assays using 36–base pair (bp) double-stranded DNA (dsDNA) containing multiple CpG sites as a substrate to monitor the formation of the *S*-adenosyl-L-homocysteine reaction product. A 40–amino acid histone H3 tail peptide (residues 1 to 40) harboring methylated or unmethylated K4/K36 was incubated with the DNMT3B-3L complex before measuring enzymatic activity. In the presence of the H3K4^{me0}K36^{me0} peptide, 3BΔ214-3L activity was slightly increased, whereas in the presence of H3K4^{me3}K36^{me0}, its activity remained almost unchanged relative to that of H3-free 3BΔ214-3L (Fig. 1A). However, in the presence of the H3K4^{me3}K36^{me3} peptide with a trimethylated K36, 3BΔ214-3L activity increased approximately twofold, and in the presence of the H3K4^{me0}K36^{me3} peptide, its activity was even more markedly enhanced (by ~3.5-fold) (Fig. 1A). This result shows that unmethylation of K4 and trimethylation of K36 in the histone H3 peptide exert synergistic effects in up-regulating the methyltransferase activity of 3BΔ214-3L.

Next, we compared the activity of the 3BΔ214-3L and 3BΔ412-3L complexes, i.e., with or without the PWWP domain, respectively, in the absence or presence of the most stimulatory H3K4^{me0}K36^{me3} peptide. We found that 3BΔ412-3L activity was not stimulated by the H3K4^{me0}K36^{me3} peptide, whereas 3BΔ214-3L complex activity was highly up-regulated (Fig. 1B). This outcome is consistent with previous in vivo data showing that the presence of the PWWP domain within DNMT3B and methylation of K36 in H3 are both required for DNMT3B-mediated methylation of actively transcribed genes (*17*). Collectively, our biochemical results demonstrate that a specific modified histone H3 tail peptide with an unmethylated K4 and a trimethylated K36 (H3K4^{me0}K36^{me3}) profoundly enhances the methyltransferase activity of the 3BΔ214-3L complex, and this effect is dependent on the presence of the PWWP domain within DNMT3B.

A crystal structure of the PWWP domain reveals the basis for H3-assisted up-regulation

To investigate the mechanism underlying how the PWWP domain up-regulates DNMT3B activity, we measured by fluorescence polarization the DNA binding affinities of DNMT3B-3L complexes using fluorophore-labeled 30-bp DNA as a substrate. In the presence of the most stimulatory peptide, i.e., H3K4^{me0}K36^{me3}, the 3BΔ214-3L complex displayed the highest binding affinity for DNA, with a dissociation constant (K_d) of 0.85 ± 0.07 μM, relative to the weaker DNA binding affinities observed for 3BΔ214-3L in the absence of an H3 peptide (K_d = 3.51 ± 0.28 μM) or in the presence of an H3K4^{me0}K36^{me0} peptide (K_d = 2.34 ± 0.15 μM), an H3K4^{me3}K36^{me0} peptide (K_d = 3.50 ± 0.30 μM), or an H3K4^{me3}K36^{me3} peptide (1.39 ± 0.12 μM) (Fig. 2A).

Moreover, the PWWP domain alone exhibited a low binding affinity for DNA (K_d = 344.50 ± 44.61 μM) (Fig. 2B), supporting a previous finding that the PWWP domain of DNMT3B is involved in nonspecific DNA binding (*22*). In the presence of the H3K36^{me3} peptide, the DNA binding affinity of the PWWP domain was increased by 38-fold with a K_d of 9.12 ± 0.67 μM. These results indicate that the DNA binding affinity of the 3BΔ214-3L complex is increased and that the PWWP domain is involved in DNA binding in the presence of the H3K4^{me0}K36^{me3} peptide.

To gain further insights into the increased DNA binding affinity of the PWWP domain through H3 peptide interactions, we crystallized PWWP and the PWWP-H3 peptide complex in the presence or absence of DNA oligonucleotides of various lengths. However, all of the PWWP-H3, PWWP-DNA, and PWWP-H3-DNA cocrystals poorly diffracted x-rays, with only the crystals of the PWWP domain alone diffracting x-rays to an acceptable resolution of 2.74 Å, i.e., feasible for crystal structure determination. The crystals of the apo-form PWWP exhibited an identical space group and unit cell dimensions to the crystal structure reported previously of the PWWP domain bound with a 12–amino acid H3K36^{me3} peptide [Protein Data Bank (PDB) code: 5CIU] (*23*). Our crystal structure of the apo-form PWWP domain, containing two molecules per asymmetric unit, was refined to an *R*-factor/*R*-free of 22.08/26.72 for 13,059/1311 reflections (Fig. 2, C and D, and table S1). The structure of the apo-form PWWP domain determined in the current study (PDB code: 8ZLK) folds into a Tudor domain of a five-stranded antiparallel β-barrel packed against an α-helical region, i.e., similar to overall folding of the H3-bound PWWP reported previously (PDB entry: 5CIU) (*23*), as well as folding of the PWWP domain of mouse dnmt3b (PDB entry: 1KHC) (*22*). Superimposition of the apo-form of mouse and human PWWP structures gave a root mean square deviation (RMSD) of 1.04 Å for 128 Cα atoms. Superimposition of the apo-form and H3-bound PWWP domain structures yielded an RMSD of 0.38 Å for 120 Cα atoms, indicating that H3 peptide binding does not induce an overall conformational change in the PWWP domain (Fig. 2C). Although the RMSD between human and mouse PWWP domains is low, the side-chain orientations of several residues, likely involved in H3 tail and DNA binding, differ extensively, including Lys^{232}, Lys^{251}, and Asp^{266} in the human PWWP domain (fig. S2). These findings suggest that these residues exhibit flexibility, and H3 tail binding may alter their orientations, thereby modifying the surface potential of the PWWP domain to enhance DNA binding affinity.

On the basis of the previously reported cryo-EM structure of the PWWP domain of the transcriptional coactivator LEDGF bound with a nucleosome (*26*), it has been suggested that the DNA binding surface of the PWWP domain is located proximal to the H3-binding region. Upon close examination of the H3-binding regions of our crystal structure, we noticed that the side-chain orientation of Asp^{266} that is located close to the H3 peptide varies markedly. The

A

3BΔ214-3L	K_d (μM)	R^2
w/o H3	3.51 ± 0.28	0.9862
w/ H3K4^{me0}K36^{me0}	2.34 ± 0.15	0.9894
w/ H3K4^{me3}K36^{me0}	3.50 ± 0.30	0.9842
w/ H3K4^{me3}K36^{me3}	1.39 ± 0.12	0.9813
w/ H3K4^{me0}K36^{me3}	0.85 ± 0.07	0.9805

B

PWWP	K_d (μM)	R^2
WT	344.50 ± 44.61	0.9827
WT w/ H3K36^{me3}	9.12 ± 0.67	0.9956
K268A	736.80 ± 86.84	0.9928
K268A w/ H3K36^{me3}	24.31 ± 2.00	0.9967

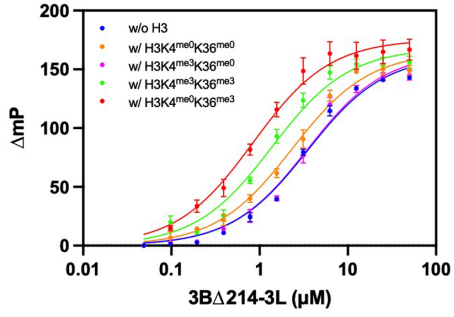

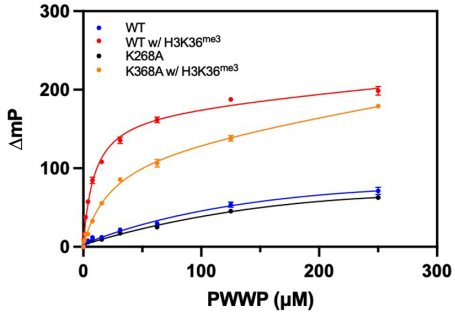

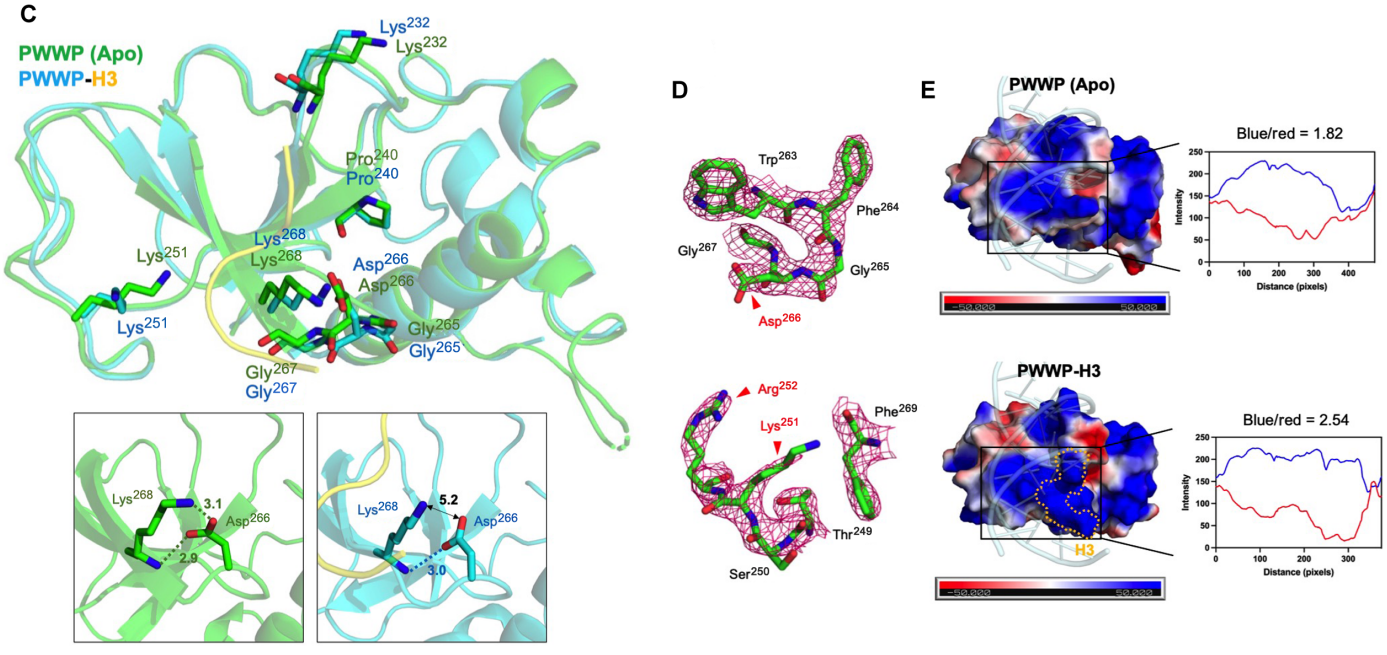

Fig. 2. The PWWP domain in the DNMT3B-3L complex is involved in DNA binding upon interactions with the H3K4^{me0}K36^{me3} peptide. (**A**) The DNA binding affinities of the 3BΔ214-3L complex in the absence and presence of the H3 tail peptide were measured by fluorescence polarization spectroscopy. (**B**) The DNA binding affinities of the PWWP domain and PWWP-K268A mutant in the absence and presence of the H3K4^{me0}K36^{me3} peptide were measured by fluorescence polarization spectroscopy. Data are plotted as means ± SD from three independent experiments and fitted using GraphPad Prism version 9. (**C**) Superimposition of the crystal structures of apo-form PWWP (this study; PDB entry: 8ZLK) and H3-bound PWWP (PDB entry: 5CIU) reveals that the hydrogen bonding network between Asp^{266} and Lys^{268} is different in the two structures. (**D**) Omit Fourier ($2F_o - F_c$) maps surrounding residues Asp^{266} (top panel) and Lys^{251} (bottom panel) contoured at 2.0 σ. (**E**) Electrostatic surface potential around the H3-binding region of the apo-form and H3-bound PWWP structures. The locations of the bound DNA (pale blue structure) and H3 peptide (marked by a dashed line) are displayed on the surfaces. The averaged ratios of electropositive (blue) to electronegative (red) areas analyzed by ImageJ software are shown above the plots.

Asp^{266} ($O_{\delta1}$) side chain forms a hydrogen bond with the side chain of Lys^{268} (N_ζ) in the apo-form of PWWP, but this hydrogen bond is absent from the structure of H3-bound PWWP (Fig. 2C). Consequently, the Lys^{268} side chain is reoriented in this latter, pointing outward from the PWWP surface. Furthermore, the Lys^{251} side chain is also differentially orientated in the apo-form and H3-bound PWWP structures, pointing outward from the surface of the latter but inward for the former (Fig. 2C). The K295E and K295I mutations in DNMT3A disrupt DNA interactions and are associated with paraganglioma, a rare neuroendocrine neoplasm (*27*). K295 in DNMT3A corresponds to K232 in DNMT3B, which is located closely to the modeled DNA. These protruding side chains of the positively charged Lys^{232}, Lys^{251}, and Lys^{268} may contribute to the increased DNA binding affinity displayed by the PWWP domain upon H3 binding. To validate this hypothesis, we constructed and purified the PWWP domain containing the K268A mutation. The PWWP-K268A mutant exhibited a 2.1-fold decrease in DNA binding affinity (K_d = 736.80 ± 86.84 μM) compared to the wild-type

PWWP domain ($K_d = 344.50 \pm 44.61$ μM) (Fig. 2B). When tested in the presence of the H3K36^{me3} peptide, the PWWP-K268A mutant showed a 2.7-fold decrease in DNA binding affinity ($K_d = 24.31 \pm 2.0$ μM) relative to the wild-type PWWP domain ($K_d = 9.12 \pm 0.67$ μM). These findings confirm that Lys^{268} plays a crucial role in the H3K36^{me3} peptide–enhanced DNA binding of the PWWP domain.

We further calculated electrostatic surface potentials around the H3-binding regions of the apo-form and H3-bound PWWP structures. Our analysis of the ratio of electropositive (blue) to electronegative (red) areas indicates that the H3-bound PWWP domain is 1.4 times more electropositive than the apo-form on the predicted DNA binding surfaces (Fig. 2E). Apart from the protruding basic-charged side chains, electronegative oxygen atoms in the backbone of Pro^{240}, Gly^{265}, Gly^{267}, and Asp^{266} are also masked by the H3 peptide in the H3-bound PWWP structure (Fig. 2C). Together, these biochemical and structural data reveal that binding of the H3 peptide to the PWWP domain of DNMT3B increases its basic-charged surface, thereby enhancing its DNA binding affinity.

The H3K4^{me0}K36^{me3} peptide induces active conformational changes in the DNMT3B-3L complex

To investigate the mechanism underlying the interplay between DNMT3B and the H3K4^{me0}K36^{me3} peptide, we used SAXS to elucidate the overall shape and conformation of DNMT3B-3L in solution. The protein sample at different concentrations was subjected to size-exclusion chromatography coupled with SAXS (SEC-SAXS) (fig. S3). The same fractions eluted from the size exclusion chromatography column were simultaneously examined by synchrotron SAXS, which gave the molecular weights and the maximum dimensions of the protein samples (Fig. 3 and fig. S3). The distance distribution functions [$P(r)$] and Guinier fit revealed maximum dimensions and radii of gyration (R_g) of 64.0 and 17.5 Å for the PWWP domain, 159.2 and 44.6 Å for 3BΔ412-3L, and 212.4 and 51.8 Å for 3BΔ214-3L, respectively (Fig. 3). In the presence of the H3 peptide, the maximum dimensions and R_g of the PWWP domain (73.5 and 17.7 Å) and 3BΔ412-3L (160.2 and 44.9 Å) changed slightly. However, in the presence of the H3K4^{me0}K36^{me3} peptide, the maximum dimension of 3BΔ214-3L under the same condition declined greatly from 212.4 to 189.4 Å, indicating that structural changes had been induced by the presence of the H3 peptide (Fig. 3, B and C).

The SAXS structural envelope for 3BΔ412-3L and 3BΔ214-3L calculated using GASBOR further revealed that the H3 peptide induced conformational changes in the enzyme complex. The simulated scattering intensities (shown in colored lines) generated from the envelopes fitted well with the experimental data (black dots) with low χ^2 values of 1.0 to 2.2 (Fig. 3, A to C). Molecular models of 3BΔ412-3L were built using the crystal structures of the DMNT3A-3L complex in autoinhibitory and active conformations (*20*) as templates. In the absence of the H3 peptide, the 3BΔ412-3L SAXS envelope fitted well with the structural model of 3BΔ412-3L in the autoinhibitory conformation with the ADD domain located in the "UP" position, which may block the DNA binding region in the CD. In the presence of the H3K4^{me0}K36^{me0} peptide, the SAXS envelope fitted well with the structural model of 3BΔ412-3L in the active conformation with the ADD domain shifted to the "DOWN" position (Fig. 3B). The rigid-body models of the PWWP domain (this study; PDB code: 8ZLK) and the structural model of the 3BΔ412-3L complex were further fitted into the SAXS envelope of the 3BΔ214-3L complex. The SAXS envelope of the 3BΔ214-3L complex revealed an additional density, potentially representing the location of the PWWP domain that is also rearranged in the presence of the H3K4^{me0}K36^{me3} peptide and indicating that the PWWP domain also shifts its position through interactions with the H3 peptide (see dashed circles in Fig. 3C).

The distance distribution functions [$P(r)$] of the 3BΔ214-3L complex exhibited a characteristic smoothing toward 0 as the r value approached D_{max} (Fig. 3C), and the dimensionless Kratky plot revealed that the curve peak at q^*R_g was slightly greater than $\sqrt{3}$ (fig. S3D), indicating that 3BΔ214-3L exhibited some degree of flexibility (*28*, *29*). To gain further insights into its molecular mobility, we modeled the structure of the 3BΔ214-3L complex in the absence and presence of the H3K4^{me0}K36^{me3} peptide by the ensemble optimization method (EOM) (*30*). The EOM algorithm selected coexisting conformers from large pools of conformations, and the resulting SAXS profile calculated from the subensembles fitted well with measured SAXS profiles having low χ^2 values (Fig. 4A). Using EOM, four major conformations emerged consistently with high frequencies across three independent analyses, including two autoinhibitory forms and two activated forms (with the peaks corresponding to these four conformations labeled in Fig. 4B). It was estimated that in the absence of the H3 peptide, 3BΔ214-3L predominantly adopted two autoinhibitory conformations with the ADD domain in the UP position (46.0 to 46.4% in Autoinhibitory Form 1 and 31.0 to 32.4% in Autoinhibitory Form 2), and the remaining 21.5 to 23.0% adopted the active conformation with the ADD domain in the DOWN position (Activated Form 1) (Fig. 4C). In the presence of the most stimulatory H3K4^{me0}K36^{me3} peptide, all of the 3BΔ214-3L complexes were shifted to active conformations, with 29.3 to 29.6% in Activated Form 1 and 70.4 to 70.7% in Activated Form 2 (Fig. 4C).

The SAXS model of 3BΔ214 in Activated Form 2 exhibits a domain arrangement that closely resembles the molecular models of DNMT3B predicted by AlphaFold 2 (Fig. 5A and fig. S4A). In this active conformation, the PWWP domain is integrated into the 3BΔ214-3L complex and directly engages with the ADD domain. Moreover, in this SAXS model (in Activated Form 2), the PWWP domain and CD simultaneously interact with DNA, similar to the AlphaFold 3–predicted model of the DNMT3B-3L-DNA complex (fig. S4B) (*31*). Together, these results indicate that our SAXS structural model in the active conformation (Fig. 5A) may represent an epigenetic assembly of the DNMT3B-DNMT3L-H3 peptide-DNA complex in the chromatin-associated premethylation state.

To determine whether this interaction between the PWWP domain and the ADD domain occurs in the presence of the H3K4^{me0}K36^{me3} peptide, we performed glutathione *S*-transferase (GST) pull-down assays using a GST-tagged ADD domain to pull down the PWWP domain. Without the H3K4^{me0}K36^{me3} peptide, the GST-tagged ADD domain failed to pull down the PWWP domain. However, in the presence of the H3 peptide, the ADD domain pulled down the PWWP domain (Fig. 5B). In addition, we generated a mutated version of the GST-tagged ADD domain containing a D470A substitution. D470 in DNMT3B corresponds to D529 in DNMT3A, where the D529A mutation disrupts DNMT3A-H3 peptide interactions (*20*). In our pull-down assays, this ADD-D470A mutant failed to interact with the PWWP domain, regardless of the presence or absence of the H3K4^{me0}K36^{me3} peptide (Fig. 5B). These findings suggest that the binding of the H3K4^{me0}K36^{me3} peptide triggers a conformational change in the 3BΔ214-3L complex, allowing the PWWP domain to directly associate with the ADD domain, where

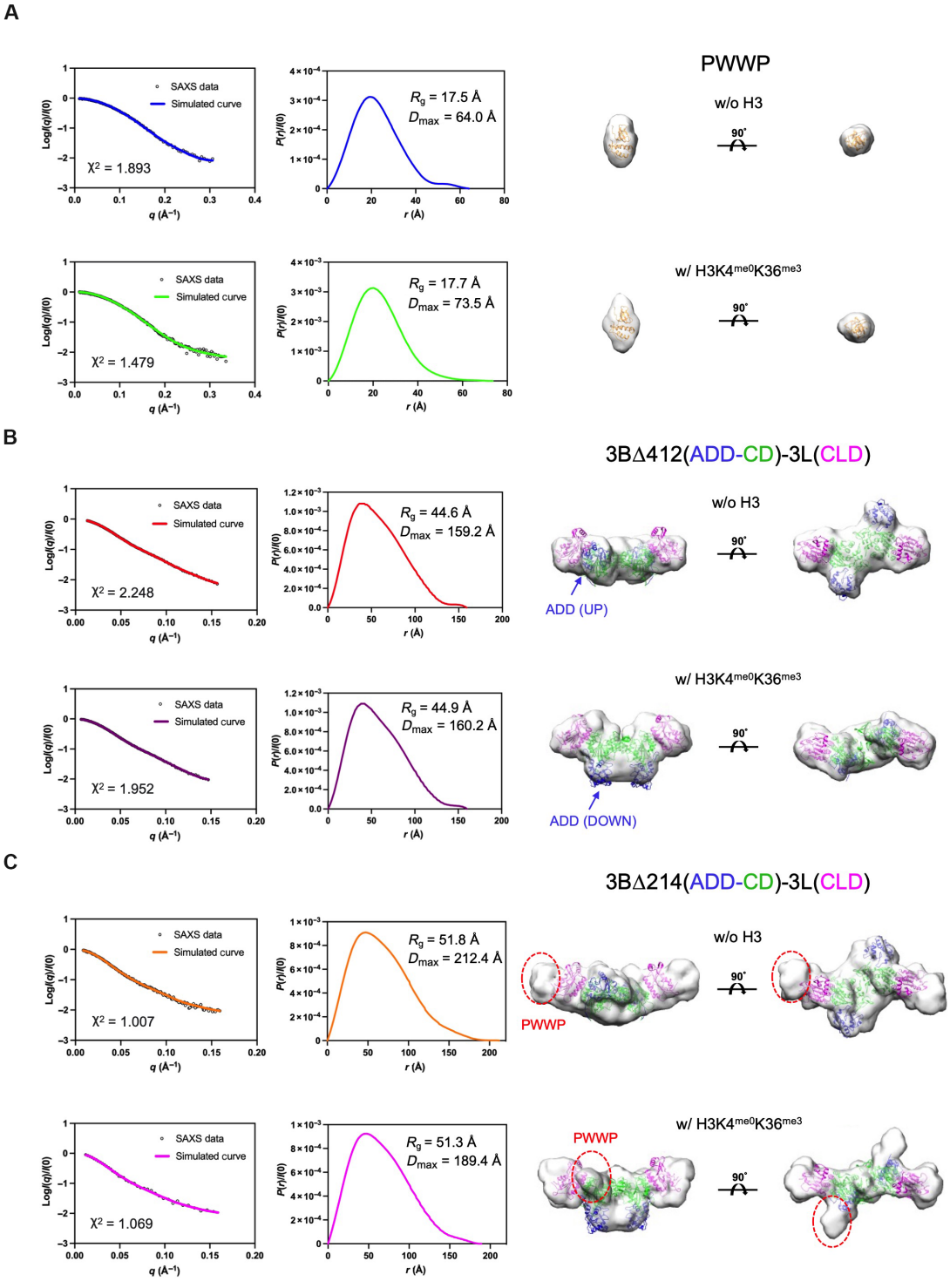

Fig. 3. Solution SAXS structures of the DNMT3B-3L complexes in the absence or presence of the H3 peptide. SAXS profiles (black dots) are represented as logarithmic scattering intensities in the left panels. Calculated profiles are displayed as solid-colored lines, with the fitting errors (χ^2) shown within the figure. Distance distribution functions [$P(r)/I(0)$] are shown in the middle panels with radii of gyration (R_g) and maximum diameters (D_{max}) shown within the figures. SAXS envelopes of (**A**) the PWWP domain, (**B**) 3BΔ412-3L, and (**C**) 3BΔ214-3L were determined using GASBOR (dashed circles mark the possible location of the PWWP domain). Rigid domains were used to fit into the SAXS envelope: the PWWP domain (this study; PDB: 8ZLK) and the 3BΔ412-3L structural model [built on the basis of the structures of the DNMT3A-3L complex in autoinhibitory and active conformations (*20*)]. The ADD and PWWP domains are substantially shifted in the 3BΔ412-3L and 3BΔ214-3L complexes in the presence of the H3K4^{me0}K36^{me0} and H3K4^{me0}K36^{me3} peptides, respectively.

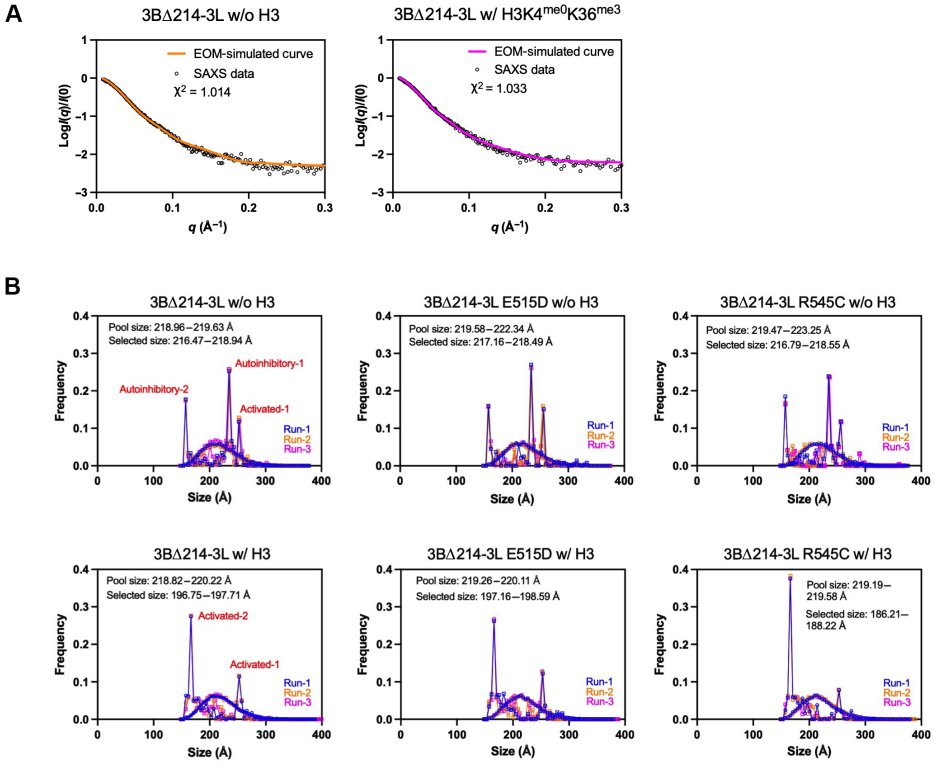

	Autoinhibitory Form 1	Autoinhibitory Form 2	Activated Form 1	Activated Form 2
3BΔ214-3L				
w/o H3	**46.0–46.4%**	**31.0–32.4%**	**21.5–23.0%**	**0%**
w/ H3K4me0K36me3	**0%**	**0%**	**29.3–29.6%**	**70.4–70.7%**
3BΔ214-3L E515D				
w/o H3	**45.2–46.5%**	**27.4–27.6%**	**23.4–27.6%**	**0%**
w/ H3K4me0K36me3	**0%**	**0%**	**31.8–32.4%**	**67.6–68.2 %**
3BΔ214-3L R545C				
w/o H3	**44.1–45.6%**	**31.6–34.1%**	**21.8–24.2%**	**0%**
w/ H3K4me0K36me3	**0%**	**0%**	**16.8–17.6%**	**82.4–83.2%**

Fig. 4. The DNMT3B-3L complex is dynamic and adopts multiple conformations. (**A**) SAXS profiles of the 3BΔ214-3L complex (black dots) in the absence (left panel) or presence (right panel) of the H3K4^{me0}K36^{me3} peptide. The SAXS data were analyzed by the EOM and the EOM-simulated curves (solid lines) that were calculated from a group of conformers have been fitted with the SAXS data with low χ^2 values. (**B**) The frequencies of size distribution that resulted from three independent EOM analyses (labeled by Run-1, Run-2, and Run-3) reveal four major conformations with high frequencies. The peaks that correspond to Autoinhibitory-1, Autoinhibitory-2, Activated-1, and Activated-2 conformations are labeled in the figure. (**C**) Percentage ranges of multiple conformations (Autoinhibitory Form 1, Autoinhibitory Form 2, Activated Form 1, and Activated Form 2) of wild-type 3BΔ214-3L, as well as the two mutant complexes (E515D and R545C), generated from three independent EOM analyses in the absence or presence of the H3K4^{me0}K36^{me3} peptide are shown.

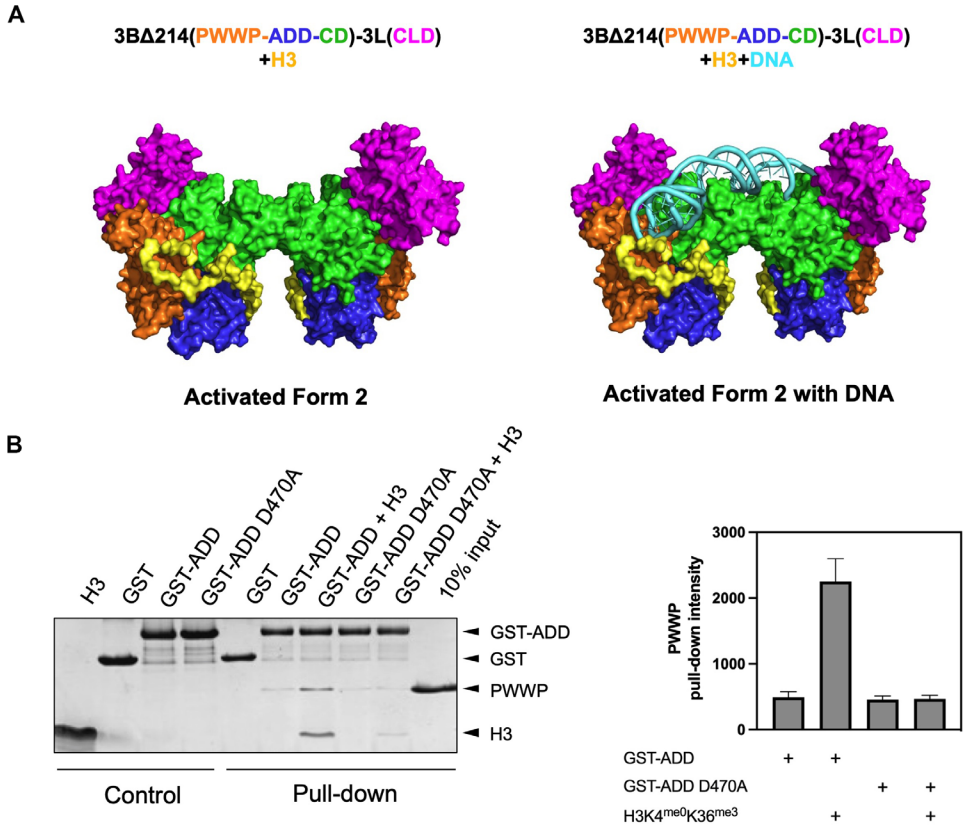

Fig. 5. The PWWP domain of DNMT3B directly interacts with the ADD domain upon H3 peptide binding. (**A**) Structure model of the 3BΔ214-3L complex (SAXS model in Activated Form 2) bound with an H3 peptide (left panel) and structural model of the 3BΔ214-3L-H3 peptide complex bound with DNA (right panel). (**B**) In the absence of the H3K4^{me0}K36^{me3} peptide, GST pull-down assays show that the GST-tagged ADD domain failed to pull down the PWWP domain. However, in the presence of the H3K4^{me0}K36^{me3} peptide, the GST-tagged ADD domain pulled down the PWWP domain. The ADD mutant D470A failed to pull down the PWWP domain in the presence or absence of the H3K4^{me0}K36^{me3} peptide. The assays were quantified by band densitometry and plotted as the means ± SD for three independent experiments (right panel).

D470 plays a key role in ADD-H3 peptide interactions. Overall, the EOM analysis and biochemical assays suggest that the H3K4^{me0}K36^{me3} peptide induces a substantial conformational change in the 3BΔ214-3L complex, with both the ADD and PWWP domains shifting their positions from autoinhibitory to active conformations (see movie S1).

Oncogenic R545C mutation enhances DNMT3B's activity upon interactions with the H3K4^{me0}K36^{me3} peptide

Alterations in *DNMT3B* expression or mutations in the enzyme have been implicated in various types of cancer, such as a recent study showing that certain mutations of *DNMT3B* are associated with prostate cancer (*32*). That study reported that 22% of metastatic castration-resistant prostate cancers presented an epigenomic subtype characterized by excessive methylation and somatic mutations in *TET2*, *DNMT3B*, *IDH1*, and *BRAF* (*32*). Nevertheless, it was unclear how two mutations of *DNMT3B*, i.e., E515D and R545C, contribute to global genome-wide hypermethylation and prostate cancer since both mutation sites are located within the ADD domain that is not directly involved in H3 peptide binding and complex assembly (Fig. 6A). To gain further insights, first, we expressed and purified the 3BΔ214-3L and 3BΔ412-3L complexes harboring the E515D or R545C mutation (fig. S1). Circular dichroism profiles of the two resulting mutant complexes, 3BΔ214(E515D)-3L and 3BΔ214(R545C)-3L, were unchanged relative to those of the wild-type 3BΔ214-3L complex, indicating that the mutations did not cause major structural perturbations in terms of overall protein folding and complex assembly (fig. S5).

To reveal whether the E515D and R545C mutations affect enzymatic activity, we assayed the methyltransferase activities of the wild-type and mutant 3BΔ412-3L and 3BΔ214-3L complexes. In comparison to the methyltransferase activity of the wild-type 3BΔ412-3L complex (set to 1.0), the E515D mutant displayed similar relative activities in the absence and presence of the H3K4^{me0}K36^{me0} peptide (Fig. 6B). However, the R545C mutant exhibited greater activity than the wild-type complex in the presence of the H3K4^{me0}K36^{me0} peptide. In contrast, in the presence of the H3K4^{me3}K36^{me0} peptide hosting a methylated K4, the activities of all three 3BΔ412-3L complexes were considerably reduced, supporting the notion that only the H3 peptide with an unmethylated K4 effectively interacts with the ADD domain and thus stimulates the activity of DNMT3B.

For the 3BΔ214-3L complexes, the H3K4^{me0}K36^{me0} peptide slightly enhanced the activities of wild-type enzyme (set to 1) and the corresponding E515D mutant, but it more strongly increased the activity of the corresponding R545C mutant (Fig. 6B). The H3K4^{me0}K36^{me3} peptide with a trimethylated K36 similarly enhanced the activities of both the wild-type and E515D mutant complexes, but notably, it

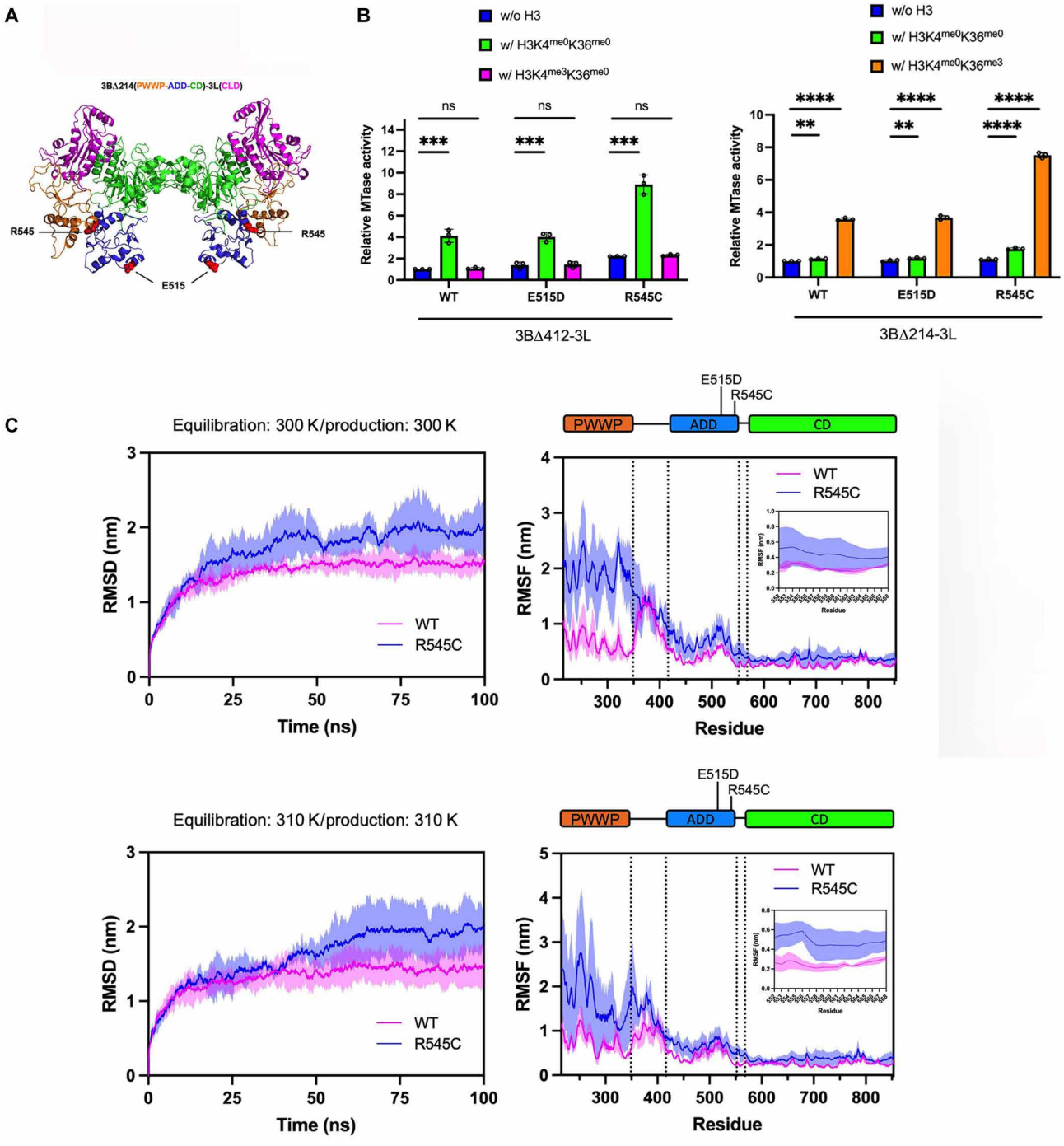

Fig. 6. Oncogenic R545C mutation enhances DNMT3B's activity upon interactions with the H3 peptide because of increased flexibility at PWWP and ADD domains. (**A**) The locations of the two mutations, E515D and R545C, on the surface of the ADD domain are displayed as ball models in the structure of the 3BΔ214-3L complex in the active conformation. (**B**) Left panel: relative methyltransferase activities of wild-type 3BΔ412-3L (set to 1) and two corresponding E515D and R545C mutant variants in the absence or presence of the H3K4^{me0}K36^{me0} peptide. Right panel: relative methyltransferase activities of the wild-type 3BΔ213-3L complex (set to 1) and two E515D and R545C mutant variants in the absence or presence of the H3K4^{me0}K36^{me3} peptide. Error bars denote SD. Statistical significance (*P* values) was determined by two-tailed Student's *t* test: $^{**}P < 0.01$, $^{***}P < 0.001$, and $^{****}P < 0.0001$. (**C**) Three independent all-atom molecular dynamics stimulations of 3BΔ214-3L-H3 complexes in the active state (Activated Form 2) for wild-type (WT) 3BΔ214-3L and mutated R545C complexes were performed in explicit solvent for 100 ns at 300 and 310 K, respectively. The dynamics of the PWWP and ADD domains were increased in the R545C mutant, which exhibited higher RMSF values in these regions than those of the wild-type 3BΔ214-3L complex. The averaged RMSD (between the initial and simulated structures) profiles and RMSF (for the residues that fluctuate from their original mean positions) profiles from three independent runs are displayed in solid red and blue lines with the error bar representing 1 SD showing in red and blue shades for wild-type and R545C mutant complexes, respectively. The RMSF profile in the loop region between the ADD domain and CD is enlarged at the right upper corner, revealing higher fluctuations in the R545C mutant complex.

exerted the strongest stimulatory effect on the R545C mutant (Fig. 6B). These results indicate that even though the R545C mutation is located in the ADD domain, it may promote interactions between the PWWP domain and the H3 peptide to strongly enhance DNMT3B's enzymatic activity. Thus, the methyltransferase activity of the DNMT3B-3L complex harboring the prostate cancer–linked R545C mutation is more markedly enhanced than its wild-type counterpart upon interactions with the H3K4^{me0}K36^{me3} peptide.

Oncogenic R545C mutation increases the propensity of DNMT3B to adopt the active conformation

To investigate the mechanism underlying the heightened activity of DNMT3B arising from its R545C mutation, we measured the SAXS profiles of 3BΔ214-3L complexes harboring either the R545C or E515D mutation in the absence or presence of the H3 peptide. The distance distribution functions [$P(r)$] and dimensionless Kratky plots indicated that both mutants exhibited flexibility (fig. S6), so we modeled the SAXS structures of the mutant complexes by EOM. In the absence of the H3 peptide, the two mutants primarily adopted autoinhibitory conformations (E515D: Autoinhibitory Form 1 = 45.2 to 46.5%, Autoinhibitory Form 2 = 27.4 to 27.6%; R545C: Autoinhibitory Form 1 = 44.1 to 45.6%, Autoinhibitory Form 2 = 31.8 to 34.1%) (see Fig. 4C). In the presence of the H3K4^{me0}K36^{me3} peptide, 67.6 to 68.2% of the E515D mutant complex shifted to Activated Form 2, i.e., similar to the proportion (70.4 to 70.7%) of wild-type enzyme that did so. This result is consistent with our methyltransferase activity assays showing that the activity of the 3BΔ214(E515D)-3L mutant complex is similar to that of wild-type enzyme in the absence or presence of the H3 peptide (Fig. 6B).

In contrast to the E515D mutant, the 3BΔ214(R545C)-3L mutant complex presented a different folding distribution to wild type in the presence of the H3K4^{me0}K36^{me3} peptide, with 82.4 to 83.2% of that mutant complex adopting Activated Form 2 and 16.8 to 18.6% being in Activated Form 1 (Fig. 4C). This result suggests that 3BΔ214(R545C)-3L was more prone to shift to Activated Form 2 in the presence of H3K4^{me0}K36^{me3} peptide than the wild-type enzyme. Assuming that Activated Form 2 is the optimal active assembly for DNA binding and methylation, these findings align well with our enzymatic activity assays (Fig. 6B) showing that 3BΔ214(R545C)-3L exhibited the highest activity (Activated Form 2: 82.4 to 83.2%) relative to the wild-type 3BΔ214-3L (70.4 to 70.7%) and 3BΔ214 (R545C)-3L (67.6 to 68.2%) complexes. Thus, our SAXS results suggest that the H3K4^{me0}K36^{me3} peptide can shift a higher percentage of the 3BΔ214-3L complex harboring the R545C mutation to the active conformation than it can do for the wild-type enzyme. Accordingly, we conclude that the R545C mutation enhances the methyltransferase activity of the DNMT3B-3L complex by making it more susceptible to adopting an active conformation through interactions with the histone H3K4^{me0}K36^{me3} peptide.

To corroborate our notion that the R545C mutation enhances the mobility of the DNMT3B-3L complex, we performed molecular dynamics simulations on the wild-type 3BΔ214-3L and R545C mutant complexes. The SAXS EOM model of wild-type 3BΔ214-3L in the active state (Activated Form 2) was used as the template. An H3 tail peptide (residues 1 to 40) was added onto the model with a conformation adopted from the H3 peptide bound with the ADD domain of DNMT3L (PDB entry: 2PVC) and the H3 peptide bound to the PWWP domain of Dnmt3b (PDB entry: 5CIU) (Fig. 5A). We conducted all-atom molecular dynamics simulations on the 3BΔ214-3L-H3 complex structure in its Activated Form 2, both with or without the R545C mutation, in an aqueous environment with explicit solvent representation. Three independent simulations were performed using GROMACS at a mean temperature of 300 K (and 310 K), 1-atm pressure, and pH 7 for a total sampling period of 100 ns (*33*–*35*). Both the wild-type DNMT3B and R545C mutant structures showed low, plateaued Cα-atom RMSD (between the initial and simulated structures) profiles (<2 Å) throughout the time-course analysis, indicating convergence in the simulation trajectories (Fig. 6C). The core CDs of both wild-type DNMT3B and R545C mutant displayed consistently low Cα-atom root mean square fluctuation (RMSF; for the residues that fluctuate from their original mean positions) values (<1.0 Å), indicating minimal atomic fluctuations within the CD relative to the average simulation structure (Fig. 6C). In contrast, the N-terminal regions of the R545C mutant, particularly within the ADD and PWWP domains, exhibited increased fluctuations with higher RMSF values compared to those of wild-type DNMT3B (Fig. 6C). The R545C mutation is located in the C-terminal end of the ADD domain, i.e., at the junction between the ADD domain and the following loop. Therefore, these molecular simulations support our notion that the R545C mutation increases the dynamics of DNMT3B in the ADD and PWWP domains, which consequently becomes more susceptible to adopting the active conformation through interactions with the histone H3K4^{me0}K36^{me3} peptide, thereby eliciting heightened methyltransferase activity.

DISCUSSION

Our study showcases the interactions between the DNMT3B-3L complex and a 40–amino acid histone H3 peptide (H3K4^{me0}K36^{me3}) that are capable of triggering formation of an active DNMT3B-3L-H3 complex that is vital for DNA methylation. Our biochemical analyses highlight an ~3.5-fold increase in DNA binding and methylation activity within the active complex upon engagement with the H3K4^{me0}K36^{me3} peptide. Notably, the heightened activity of DNMT3B-3L induced by the H3 peptide is contingent upon the presence of the PWWP domain, which specifically interacts with the trimethylated K36 mark on the H3 peptide. Our SAXS models further infer the dynamic nature of the DNMT3B-3L complex, suggesting the presence of both autoinhibitory and active states. In the presence of the H3K4^{me0}K36^{me3} peptide, the ternary DNMT3B-3L-H3 complex predominately adopts an active conformation (Fig. 5A). This structural remodeling strongly correlates with the enzyme's observed increase in methylation activity in the presence of the H3 peptide, implying a direct link between the conformational change in the enzymatic complex and its enhanced functionality in methylation.

Our study has unveiled concurrent structural remodeling of the PWWP and ADD domains by the H3 peptide, transitioning from autoinhibitory to active states (Fig. 7 and movie S1). The PWWP domains of DNMT3A and DNMT3B have been recognized for decades as DNA binding domains, displaying nonspecific interactions with DNA (*22*, *36*). Crystal structures of the PWWP domains of HDGH, HRP3, and BRPF2 have elucidated its predominant interactions with the phosphate backbone of DNA at the minor or major groove, devoid of sequence specificity (*37*–*39*). Simultaneously, the PWWP domain acts as a histone reader, specifically engaging with the trimethylated K36 mark on histone H3, guiding DNMT3 enzymes to chromatin (*16*, *17*, *40*). In a cryo-EM structure of the human transcriptional coactivator LEDGF in complex with an H3K36-methylated

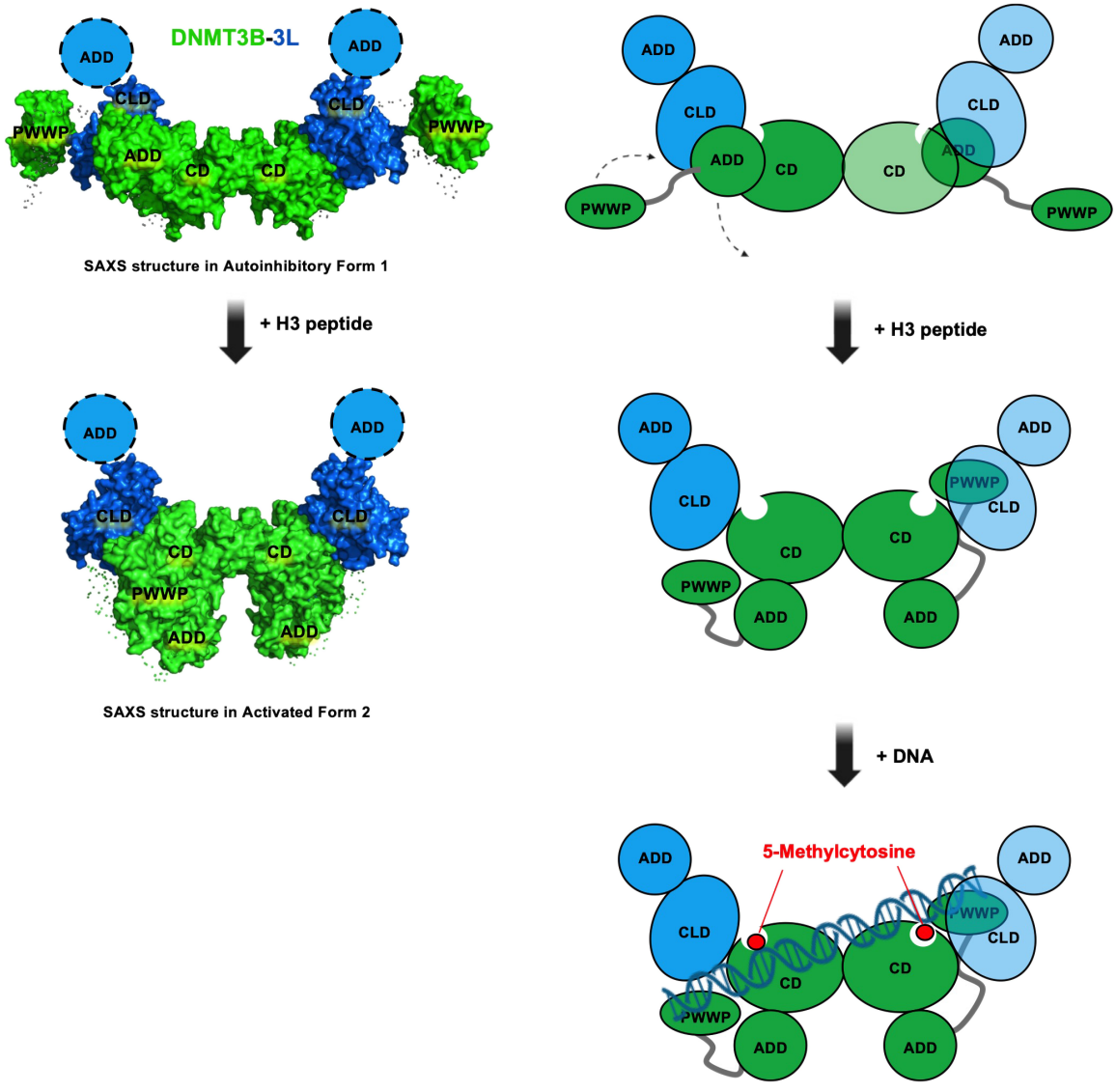

Fig. 7. Conformational rearrangement of DNMT3B triggered by H3 peptide binding unleashes its DNA binding and methylation activity. The structural model of the DNMT3B-3L complex in the absence of the H3K4^{me0}K36^{me3} peptide shows that it is primarily in the autoinhibitory state. In this autoinhibitory conformation, the ADD domain blocks the DNA binding region in the CD. Binding of the H3K4^{me0}K36^{me3} peptide to DNMT3B induces a conformational rearrangement of the PWWP and ADD domains to facilitate DNA binding and methylation. In the active state, the PWWP domain concurrently interacts with the H3 peptide and DNA. See also movie S1.

nucleosome, the PWWP domain displays multivalent binding to the methylated H3 tail and to both gyres of nucleosomal DNA (*26*). Together, these results indicate that synergistic binding of DNMT3B to the modified histone and DNA allows its preferential recruitment to H3K36-methylated genomic regions, such as CpG-dense regions and the bodies of transcribed genes, facilitating efficient DNA methylation.

In addition, our findings have revealed a noteworthy increase in the in vitro methyltransferase activity of the prostate cancer–linked DNMT3B R545C mutant relative to the wild-type enzyme. This heightened activity aligns with the observed global hypermethylation of DNA genomes in patients afflicted with cancer (*32*). This R545C mutation, positioned near the end of the ADD domain in the loop region, instigates enhanced DNMT3B dynamics, particularly affecting the mobility of the PWWP and ADD domains. We corroborated this augmented flexibility through comprehensive SAXS analyses and molecular dynamics simulations. The DNMT3B variant carrying the R545C mutation exhibits increased adaptability, allowing it to readily transition into an active conformation for DNA methylation. Consequently, its heightened flexibility leads to abnormal hypermethylation. Thus, our study sheds light on the molecular mechanism behind the observed aberrant DNA methylation in patients with prostate cancer having the DNMT3B R545C mutation.

In conclusion, our research has unveiled the fundamental mechanism by which DNMT3B is recruited to chromosomes through histone modifications at the K4 and K36 positions. The intricate interplay among DNMT3B, histone H3, and DNA collectively orchestrates the formation of an epigenetic complex in the active conformation that is crucial for efficient DNA methylation. Any mutations within

DNMT3B or alterations in the methylation/demethylation states at the H3 tail that disrupt the formation of this active complex can compromise DNA methylation, resulting in various disease conditions.

MATERIALS AND METHODS

Protein expression and purification

The cDNA fragments encoding DNMT3BΔ214 (residues 215 to 853), DNMT3BΔ412 (residues 415 to 853), ADD (residues 392 to 554), PWWP (residues 206 to 355), and DNMT3L (residues 179 to 379) were amplified by polymerase chain reaction and subcloned into the overexpression vectors by similar procedures described previously (*41*). The DNA fragments encoding DNMT3BΔ214 were inserted into pSOL Expression Vectors (Lucigen), whereas the cDNAs encoding PWWP and DNMT3L were cloned respectively into a modified pET28a(+) expression vector expressing an N-terminal 6xHis-SUMO tag and a tobacco etch virus (TEV) cleavage site to generate the pSol-tev-DNMT3BΔ214, pSol-tev-DNMT3BΔ412, pET28a(+)-tev-PWWP, and pET28a(+)-tev-DNMT3L plasmids. The cDNA encoding the ADD domain was cloned into a modified pGEX4T1 vector expressing an N-terminal GST tag and a cleavable TEV site to generate pGEX4T1-tev-ADD. The E515D and R545C mutations were introduced into pSol-tev-DNMT3BΔ214 or pSol-tev-DNMT3BΔ412, whereas K268A and D470A mutations were introduced into pET28a(+)-tev-PWWP and pGEX4T1-tev-ADD, respectively, using a QuikChange site-directed mutagenesis kit (Agilent).

All expression plasmids were transformed into the bacterial strain Rosetta2 (DE3) pLysS. Cells were grown at 37°C in LB broth (Miller) medium containing chloramphenicol (34 μg/ml) and kanamycin (50 μg/ml) for expression of pSol-tev-DNMT3BΔ214, pSol-tev-DNMT3BΔ412, and pET28a(+)-tev-PWWP or ampicillin for expression of pGEX4T1-tev-ADD (*41*). Expression of DNMT3BΔ214 and DNMT3BΔ412 (including wild-type truncated enzyme, as well as the E515D and R545C mutant variants) was induced by addition of 0.1% rhamnose. In contrast, expression of PWWP and DNMT3L was induced by 0.4 mM isopropyl-thio-β-D-galactoside until an optical density at 600 nm of 0.6 had been attained (*41*). After induction, the cells were grown at 18°C overnight and harvested by centrifugation at 6000 rpm at 4°C for 30 min. The pellet was collected and redissolved in lysis buffer containing 25 mM Hepes (pH 7.4), 500 mM NaCl, 5% glycerol, 0.5 mM tris(2-carboxylethyl)phosphine (TCEP), and EDTA-free protease inhibitor cocktail (Roche, Switzerland). The redissolved soups of DNMT3BΔ214 or DNMT3BΔ412 were mixed with the redissolved soup of DNMT3L in a 4:1 ratio to generate the DNMT3BΔ214-3L (wild-type, E515D, R545C) and DNMT3BΔ412-3L (wild-type, E515D, R545C) complexes.

Recombinant DNMT3B-3L complexes were purified by similar chromatographic methods as previously described (*41*). The pellet mixture was lysed using a microfluidizer. After centrifugation at 17,000*g* for 45 min at 4°C, the supernatant was loaded through a HisTrap FF column (GE Healthcare). After equilibrium with nickel wash buffer containing 50 mM sodium phosphate (pH 8.0), 500 mM NaCl, 5% glycerol, 5 mM β-mercaptoethanol, and 40 mM imidazole, the His-tagged protein was eluted with nickel elution buffer (same constitution as nickel wash buffer) and up to 500 mM imidazole. The 6xHis-tag was removed by TEV protease during dialysis overnight at 4°C against a buffer containing 50 mM sodium phosphate (pH 8.0), 300 mM NaCl, 5% glycerol, and 10 mM β-mercaptoethanol. The dialyzed protein sample was loaded into a HisTrap FF column (GE Healthcare), and the flow-through fractions containing the cleaved untagged protein of interest were collected. To further purify the protein sample, HiTrap Heparin HP (GE Healthcare) and gel filtration (Superdex 200 increase 10/300 GL, GE Healthcare) columns were used sequentially. The final purified samples of the DNMT3B-3L complexes were solubilized in gel filtration buffer containing 20 mM tris-HCl (pH 7.4), 200 mM NaCl, 5% glycerol, and 0.5 mM TCEP.

To purify the PWWP domain (wild type and the K268A mutant), after removing insoluble pellets by centrifugation, the supernatant was loaded onto a HisTrap FF column (GE Healthcare). After equilibrium with nickel wash buffer containing 20 mM Hepes (pH 7.4), 500 mM NaCl, 5% glycerol, and 25 mM imidazole, the His-tagged protein was eluted with nickel elution buffer (same constitution as nickel wash buffer) and up to 500 mM imidazole. The 6xHis-tag was removed by TEV protease during dialysis overnight at 4°C against a buffer containing 20 mM sodium phosphate (pH 7.4) and 250 mM NaCl. The dialyzed protein sample was loaded into a HisTrap FF column (GE Healthcare), and the flow-through fractions containing the cleaved untagged protein of interest were collected. To further purify the protein sample, HiTrap SP HP (GE Healthcare) and gel filtration (Superdex 200 increase 10/300 GL, GE Healthcare) columns were used sequentially. The final purified samples of the DNMT3B-3L complexes were solubilized in gel filtration buffer containing 20 mM Pipes (pH 6.5), 200 mM NaCl, and 5% glycerol.

To purify the GST-tagged ADD domain (wild type and the D470A mutant), after removing insoluble pellets by centrifugation, the supernatant was loaded onto a GSTrap FF column (GE Healthcare). After equilibrium with a wash buffer containing 20 mM tris-HCl (pH 8.0), 150 mM NaCl, 0.01 mM $ZnCl_2$, and 5 mM dithiothreitol (DTT), the GST-tagged protein was eluted with an elution buffer (same constitution as wash buffer) containing 20 mM reduced glutathione. The eluted protein was further purified by a HiTrap Q HP column (GE Healthcare) and Superdex 200 increase 10/300 GL column (GE Healthcare) sequentially. The purified protein was solubilized in gel filtration buffer containing 20 mM tris-HCl (pH 8.0), 150 mM NaCl, 0.01 mM $ZnCl_2$, and 5 mM DTT.

Circular dichroism spectroscopy

Far-ultraviolet circular dichroism spectra from 260 to 190 nm were recorded on an AVIV Circular Dichroism Spectrometer (Aviv Biomedical Inc.). All measurements were conducted in a 1-mm quartz cuvette at 25°C by similar procedures described before (*41*). The protein samples in 20 mM phosphate buffer (pH 7.4) were set to 0.4 μM for the DNMT3BΔ214-3L (wild-type, E515D or R545C) complexes. The circular dichroism spectra were processed by smoothing and baseline subtraction using built-in AVIV software. All experiments were performed in triplicate. Secondary structure compositions were estimated and analyzed using BeStSel (*42*). Thermal denaturation was carried out by monitoring circular dichroism signals at 222 nm from 10° to 95°C. T_m values were calculated using the maximum of the first derivative of the circular dichroism signal.

Methyltransferase activity assay

The methyltransferase activities of the wild-type and mutant DNMT 3BΔ214-3L and DNMT3BΔ412-3L complexes were measured using an MTase-Glo Methyltransferase Assay Kit (Promega) (*41*). The 36-bp dsDNA substrate [2 μM with a sequence of 5′-$(GAC)_{12}$-3′] was incubated with 0.2 μM protein in the presence or absence of 0.6 μM $H3K4^{me0}K36^{me0}$, $H3K4^{me0}K36^{me3}$, $H3K4^{me3}K36^{me0}$, or $H3K4^{me3}K36^{me3}$ peptide (residues 1 to 40: ARTKQTARKSTGGKAPRKQLATKAARK

SAPSTGGVKKPHR, synthesized by Synbio Tech Inc.) in a reaction buffer containing 20 mM tris-HCl (pH 8.0), 50 mM NaCl, 1 mM EDTA, 1 mM DTT, 5% glycerol, bovine serum albumin (0.1 mg/ml), and 10 μM *S*-adenosylmethionine in a volume of 4 μl at 37°C for 1 hour. The reaction was stopped by adding 1 μl of 0.5% trifluoroacetic acid for 5 min, followed by addition of 1 μl of 6× MTase-Glo reagent and incubation for 30 min. Next, 6 μl of MTase-Glo detection reagent was added and incubated for another 30 min. The luminescence signals were recorded using an EnSpire Multimode Plate reader (PerkinElmer).

Determination of DNA binding affinity by fluorescence polarization assays

Increasing concentrations (0.05 to 50 μM) of DNMT3BΔ214-3L complex were incubated with a 30-bp 3′-end fluorescein amidite–labeled dsDNA (15 nM) with a sequence of 5′-CTGAATACTACTTGC GCTCTCTAACCTGAT-3′ in the presence or absence of a 40–amino acid H3 peptide (150 μM) (H3K4^{me0}K36^{me0}, H3K4^{me0}K36^{me3}, H3K4^{me3}K36^{me0}, or H3K4^{me3}K36^{me3}) at 25°C for 30 min in a buffer containing 20 mM Hepes (pH 7.8), 50 mM NaCl, 5% glycerol, 1 mM DTT, and bovine serum albumin (0.5 mg/ml). The PWWP domain (wild type and the K268 mutant) was incubated with the same fluorescein amidite–labeled dsDNA in the presence or absence of the 12–amino acid H3K36^{me3} peptide (300 μM) (residues 30 to 41: PST GGVKKPHRY, synthesized by Synbio Tech Inc.). Fluorescence polarization measurements were performed on a SpectraMax Paradigm Multi-Mode Detection Platform at 25°C and analyzed in SoftMax Pro 7. The changes of fluorescence polarization signal (ΔmP) were calculated as mP − baseline mP, in which mP (millipolarization units) represents the fluorescence polarization value. Each reaction was performed in triplicate. The data were analyzed using nonlinear regression analysis in GraphPad Prism 9.

Protein crystallization and structural determinations

The purified PWWP domain from human DNMT3B was concentrated to 25 mg/ml and subjected to crystallization screening experiments. Protein crystals were grown by the hanging-drop vapor diffusion method by mixing 1 μl of the PWWP domain [in a buffer of 20 mM Pipes (pH 6.5), 200 mM NaCl, and 5% glycerol] and 1 μl of reservoir solution containing 0.2 M lithium sulfate monohydrate, 0.1 M 3-(cyclohexylamino)-1-propanesulfonic acid (pH 8.0), and 2 M ammonium sulfate. The crystals formed within 1 week at 283 K and were subsequently soaked in a cryoprotectant solution consisting of 25% glycerol and the reservoir solution before crystal mounting. X-ray diffraction data for the PWWP domain were collected at TLS beamline 15A and TPS beamline 05A at the National Synchrotron Radiation Research Center in Hsinchu, Taiwan. The diffraction data were processed in HKL2000.

The crystal structure of apo-form PWWP was refined in PHENIX Phaser using the model built by SWISS-MODEL as a template. The initial model was rebuilt using the program Coot, and amino acid side chains and water molecules were fitted according to $2|F_o| - |F_c|$ and $|F_o| - |F_c|$ electron density maps during repeated cycles of structural refinement in PHENIX. The data collection and structure refinement statistics are presented in table S1.

Small-angle x-ray scattering (SAXS)

Real-time SEC-SAXS data were recorded and normalized using the scattering of buffer by the TPS-13A SWAXS data reduction package at the TPS-13A beamline of the National Synchrotron Radiation Research Center in Hsinchu, Taiwan. The protein sample [100 μl; DNMT3BΔ214-3L, DNMT3BΔ214(E515D)-3L, DNMT3BΔ214(R545C)-3L, or DNMT3BΔ412-3L (5 mg/ml) with or without preincubation with the H3K4^{me0}K36^{me0} or H3K4^{me0}K36^{me3} peptide at a protein:peptide molar ratio of 1:3 at 4°C overnight or PWWP domain (10 mg/ml) in 20 mM tris-HCl (pH 8.0), 300 mM NaCl, 1 mM TCEP, and 5% glycerol] was injected into the Agilent-Bio SEC-03 300-Å column (300-Å pore size) at a flow rate of 0.02 ml/min and detected at a sample-to-detector distance of 2.5 m. An x-ray wavelength of 0.827 Å was used to collect 199 frames of 2-s exposure for DNMT3BΔ214-3L, DNMT3BΔ214(E515D)-3L, and DNMT3BΔ214(R545C)-3L; 113 frames for DNMT3BΔ412-3L; and 118 frames for PWWP. Selected frames were merged and analyzed for initial R_g estimation in the PRIMUS program or for D_{max} and $P(r)$ distance distributions in the GNOM program. The SAXS data collection and scattering-derived parameters of SAXS analyses are listed in table S2. Low-resolution ab initio envelopes of proteins were generated in GASBOR using the ATSAS web interface (*30*). The EOM was performed to analyze SAXS data using the structures of the PWWP domain (this study; PDB code: 8ZLK), ADD [PDB code: 7O45; (*43*)], and DNMT3B-3L heterotetramer [PDB code: 6KDP; (*13*)] as rigid bodies. First, we generated a total of 10,000 models, and then the SAXS profiles of these models were fitted with the measured SAXS profiles to select the best-fitting models.

GST pull-down assay

The PWWP domain (60 μg) was incubated with the GST-tagged wild-type or D470A mutant of the ADD domain (20 μg) in the presence or absence of H3K4^{me0}K36^{me3} peptide in a molar ratio of 2:1 (H3 peptide:PWWP) for 1 hour at 4°C in the binding buffer containing 20 mM tris-HCl (pH 8.0), 100 mM NaCl, 0.01% 2-mercaptoethanol, 5% glycerol, and 0.1% Triton X-100. The GST-ADD proteins were then immobilized to 40 μl of glutathione resins (GE Healthcare) for 1 hour at 4°C. After washing five times with the binding buffer, the bound proteins were resolved in 20% SDS–polyacrylamide gel electrophoresis and stained with Coomassie blue. Quantification of band intensity was performed using ImageJ.

Molecular modeling and predictions

To generate the DNMT3BΔ214-3L-DNA model (shown in Fig. 5A), a 44-bp dsDNA (5′-CAGGATGTATAATTCGGAAAAATTTTTCCGA ATTATACATCCTG-3′) was manually built onto the SAXS structure of DNMT3BΔ214-3L in Coot. The loop connecting the PWWP and ADD domains in DNMT3B was rebuilt to avoid clashes with DNA (shown in Fig. 5A). The final structural model was minimized using PHENIX. The molecular models of dimeric DNMT3BΔ214 and DNMT3BΔ214-3L in complex with a 54-bp dsDNA (5′-CAGGACAGGATGTATAATTCG GAAAAATTTTTCCGAATTATACATCCTGTCCTG-3′) were predicted using AlphaFold 2 (*44*) and AlphaFold 3 (*31*), respectively (shown in fig. S4). Models with the "top 2" confidence score for dimeric DNMT3BΔ214 and interface predicted template modeling/predicted template modeling score for DNMT3BΔ214-3L-DNA complex were selected and visualized in PyMOL.

All-atom molecular dynamics simulations

The R545C mutation was manually built into the structural model of DNMT3BΔ214-3L (in Active Form 2, shown in Fig. 5A) in Coot, followed by minimization using PHENIX. The wild-type and mutant structures were evaluated using the GROMACS 2021.5

molecular dynamics software package (*33*–*35*). The OPLS-AA/L all-atom force field (*45*) was used to parameterize the protein. The structures were solvated with spc216 water molecules and neutralized with chloride counterions. Three independent molecular dynamics simulations were performed for 100 ps, first at constant volume and temperature (*NVT*) and then at constant pressure and temperature (*NPT*). This resulted in an equilibrated system at 300 K (and 310 K) and 1 atm. The structures were subjected to an unrestrained 100-ns dynamic simulation, and the RMSD and RMSF of the protein backbone were computed using GROMACS.

Supplementary Materials

The PDF file includes:

Figs. S1 to S6
Tables S1 and S2
Legend for movie S1

Other Supplementary Material for this manuscript includes the following:

Movie S1

REFERENCES AND NOTES

1. Y. Feng, M. Endo, H. Sugiyama, Nucleosomes and epigenetics from a chemical perspective. *Chembiochem* **22**, 595–612 (2021).
2. W. Zhang, J. Xu, DNA methyltransferases and their roles in tumorigenesis. *Biomarker Res.* **5**, 1 (2017).
3. F. Lyko, The DNA methyltransferase family: A versatile toolkit for epigenetic regulation. *Nat. Genet. Rev.* **19**, 81–92 (2018).
4. H. Denis, M. N. Ndlovu, F. Fuks, Regulation of mammalian DNA methyltransferases: A route to new mechanisms. *EMBO Rep.* **12**, 647–656 (2011).
5. M. Laisné, N. Gupta, O. Kirsh, S. Pradhan, P.-A. Defossez, Mechanisms of DNA methyltransferase recruitment in mammals. *Genes* **9**, 617 (2018).
6. M. Okano, D. W. Bell, D. A. Haber, E. Li, DNA methyltransferases Dnmt3a and Dnmt3b are essential for de novo methylation and mammalian development. *Cell* **99**, 247–257 (1999).
7. F. Chedin, M. R. Lieber, C. L. Hsieh, The DNA methyltransferase-like protein DNMT3L stimulates de novo methylation by Dnmt3a. *Proc. Natl. Acad. Sci. U.S.A.* **99**, 16916–16921 (2002).
8. B. L. Wienholz, M. S. Kareta, A. H. Moarefi, C. A. Gordon, P. A. Ginno, F. Chedin, DNMT3L modulates significant and distinct flanking sequence preference for DNA methylation by DNMT3A and DNMT3B in vivo. *PLOS Genet.* **6**, e1001106 (2010).
9. I. Suetake, F. Shinozaki, J. Miyagawa, H. Takeshima, S. Tajima, DNMT3L stimulates the DNA methylation activity of Dnmt3a and Dnmt3b through a direct interaction. *J. Biol. Chem.* **279**, 27816–27823 (2004).
10. Z.-X. Chen, J. R. Mann, C.-L. Hsieh, A. D. Riggs, F. Chedin, Physical and functional interactions between the human DNMT3L protein and members of the de novo methyltransferase family. *J. Cell. Biochem.* **95**, 902–917 (2005).
11. D. Jia, R. Z. Jurkowska, X. Zhang, A. Jeltsch, X. Cheng, Structure of Dnmt3a bound to Dnmt3L suggests a model for de novo DNA methylation. *Nature* **449**, 248–251 (2007).
12. Z.-M. Zhang, R. Lu, P. Wang, Y. Yu, D. Chen, L. Gao, S. Liu, D. Ji, S. B. Rothbart, Y. Wang, G. G. Wang, J. Song, Structural basis for DNMT3A-mediated de novo DNA methylation. *Nature* **554**, 387–391 (2018).
13. C.-C. Lin, Y.-P. Chen, W.-Z. Yang, J. C. K. Shen, H. S. Yuan, Structural insights into CpG-specific DNA methylation by human DNA methyltransferase 3B. *Nucleic Acids Res.* **48**, 3949–3961 (2020).
14. L. Gao, M. Emperle, Y. Guo, S. A. Grimm, W. Ren, S. Adam, H. Uryu, Z.-M. Zhang, D. Chen, J. Yin, M. Dukatz, H. Anteneh, R. Z. Jurkowska, J. Lu, Y. Wang, P. Bashtrykov, P. A. Wade, G. G. Wang, A. Jeltsch, J. Song, Comprehensive structure-function characterization of DNMT3B and DNMT3A reveals distinctive de novo DNA methylation mechanisms. *Nat. Commun.* **11**, 3355 (2020).
15. Y. Zhang, R. Jurkowska, S. Soeroes, A. Rajavelu, A. Dhayalan, I. Bock, P. Rathert, O. Brandt, R. Reinhardt, W. Fischle, A. Jeltsch, Chromatin methylation activity of Dnmt3a and Dnmt3a/3L is guided by interaction of the ADD domain with the histone H3 tail. *Nucleic Acids Res.* **38**, 4246–4253 (2010).
16. A. Dhayalan, A. Rajavelu, P. Rathert, R. Tamas, R. Z. Jurkowska, S. Ragozin, A. Jeltsch, The Dnmt3a PWWP domain reads histone 3 Lysine 36 trimethylation and guides DNA methylation. *J. Biol. Chem.* **285**, 26114–26120 (2010).
17. T. Baubec, D. F. Colombo, C. Wirbelauer, J. Schmidt, L. Burger, A. R. Krebs, A. Akalin, D. Schubeler, Genomic profiling ofDNAmethyltransferases reveals a role for DNMT3B in genic methylation. *Nature* **520**, 243–247 (2015).
18. S. D. Taverna, H. Li, A. J. Ruthenburg, C. D. Allis, D. J. Patel, How chromatin-binding modules interpret histone modifications: Lessons from professional pocket pickers. *Nat. Struct. Mol. Biol.* **14**, 1025–1040 (2007).
19. S. K. T. Ooi, C. Qiu, E. Bernstein, K. Li, D. Jia, Z. Yang, H. Erdjument-Bromage, P. Tempst, S.-P. Lin, C. D. Alllis, X. Cheng, T. H. Bestor, DNMT3L connects unmethylated lysine 4 of histone H3 to de novo methylation of DNA. *Nature* **448**, 714–717 (2007).
20. X. Guo, L. Wang, J. Li, Z. Ding, J. Xiao, X. Yin, S. He, P. Shi, L. Dong, G. Li, C. Tian, J. Wang, Y. Cong, Y. Xu, Structural insight into autoinhibition and histone H3-induced activation of DNMT3A. *Nature* **517**, 640–644 (2015).
21. S. Qin, J. Min, Structure and function of the nucleosome-binding PWWP domain. *Trends Biochem. Sci.* **39**, 536–547 (2014).
22. C. Qiu, K. Sawada, X. Zhang, X. Cheng, The PWWP domain of mammalian DNA methyltransferase Dnmt3b defines a new family of DNA-binding folds. *Nat. Struct. Biol.* **9**, 217–224 (2002).
23. G. Rondelet, T. D. Maso, L. Willems, J. Wouters, Structural basis for recognition of histone H3K36me3 nucleosome by human de novo DNA methyltransferases 3A and 3B. *J. Struct. Biol.* **194**, 357–367 (2016).
24. T.-H. Xu, M. Liu, X. E. Zhou, G. Liang, G. Zhao, H. E. Xu, K. Melcher, P. A. Jones, Structure of nucleosome-bound DNA methyltransferases DNMT3A and DNMT3B. *Nature* **586**, 151–155 (2020).
25. J. Lu, J. Fang, H. Zhu, K. L. Liang, N. Khudaverdyan, J. Song, Structural basis for the allosteric regulation and dynamic assembly of DNMT3B. *Nucleic Acids Res.* **51**, 12476–12491 (2023).
26. H. Wang, L. Farnung, C. Dienemann, P. Cramer, Structure of H3K36-methylated nucleosome–PWWP complex reveals multivalent cross-gyre binding. *Nat. Struct. Biol.* **27**, 8–13 (2020).
27. M. Dukatz, K. Holzer, M. Choudalakis, M. Emperle, C. Lungu, P. Bashtrykov, A. Jeltsch, H3K36me2/3 binding and DNA binding of the DNA methyltransferase DNMT3A PWWP domain both contribute to its chromatin Interaction. *J. Mol. Biol.* **431**, 5063–5074 (2019).
28. P. Bernado, Effect of interdomain dynamics on the structure determination of modular proteins by small-angle scattering. *Europ. Biophys. J.* **39**, 769–780 (2010).
29. R. P. Rambo, J. A. Tainer, Characterizing flexible and intrinsically unstructured biological macromolecules by SAS using the Porod-Debye law. *Biopolymers* **95**, 559–571 (2011).
30. M. V. Petoukhov, D. Franke, A. V. Shkumatov, G. Tria, A. G. Kikhney, M. Gajda, C. Gorba, H. D. T. Mertens, P. V. Konarev, D. I. Svergun, New developments in the *ATSAS* program package for small-angle scattering data analysis. *J. Appl. Cryst.* **45**, 342–350 (2012).
31. J. Abramson, J. Adler, J. Dunger, R. Evans, T. Green, A. Pritzel, O. Ronneberger, L. Willmore, A. J. Ballard, J. Bambrick, S. W. Bodenstein, D. A. Evans, C.-C. Hung, M. O'Neill, D. Reiman, K. Tunyasuvunakool, Z. Wu, A. Žemgulytė, E. Arvaniti, C. Beattie, O. Bertolli, A. Bridgland, A. Cherepanov, M. Congreve, A. I. Cowen-Rivers, A. Cowie, M. Figurnov, F. B. Fuchs, H. Gladman, R. Jain, Y. A. Khan, C. M. R. Low, K. Perlin, A. Potapenko, P. Savy, S. Singh, A. Stecula, A. Thillaisundaram, C. Tong, S. Yakneen, E. D. Zhong, M. Zielinski, A. Žídek, V. Bapst, P. Kohli, M. Jaderberg, D. Hassabis, J. M. Jumper, Accurate structure prediction of biomolecular interactions with AlphaFold 3. *Nature* **630**, 493–500 (2024).
32. S. G. Zhao, W. S. Chen, H. Li, A. Foye, M. Zhang, M. Sjöström, R. Aggarwal, D. Playdle, A. Liao, J. J. Alumkal, R. Das, J. Chou, J. T. Hua, T. J. Barnard, A. M. Bailey, E. D. Chow, M. D. Perry, H. X. Dang, R. Yang, R. Moussavi-Baygi, L. Zhang, M. Alshalalfa, S. L. Chang, K. E. Houlahan, Y.-J. Shiah, T. M. Beer, G. Thomas, K. N. Chi, M. Gleave, A. Zoubeidi, R. E. Reiter, M. B. Rettig, O. Witte, M. Y. Kim, L. Fong, D. E. Spratt, T. M. Morgan, R. Bose, F. W. Huang, H. Li, L. Chesner, T. Shenoy, H. Goodarzi, I. A. Asangani, S. Sandhu, J. M. Lang, N. P. Mahajan, P. N. Lara, C. P. Evans, P. Febbo, S. Batzoglou, K. E. Knudsen, H. H. He, J. Huang, W. Zwart, J. F. Costello, J. Luo, S. A. Tomlins, A. W. Wyatt, S. M. Dehm, A. Ashworth, L. A. Gilbert, P. C. Boutros, K. Farh, A. M. Chinnaiyan, C. A. Maher, E. J. Small, D. A. Quigley, F. Y. Feng, The DNA methylation landscape of advanced prostate cancer. *Nat. Genet.* **52**, 778–789 (2020).
33. B. Hess, C. Kutzner, D. van der Spoel, E. Lindahl, GROMACS 4: Algorithms for highly efficient, load-balanced, and scalable molecular simulation. *J. Chem. Theory Comput.* **4**, 435–447 (2008).
34. S. Pronk, S. Pall, R. Schulz, P. Larsson, P. Bjelkmar, R. Apostolov, M. R. Shirts, J. C. Smith, P. M. Kasson, D. van der Spoel, B. Hess, E. Lindahl, GROMACS 4.5: A high-throughput and highly parallel open source molecular simulation toolkit. *Bioinformatics* **29**, 845–854 (2013).
35. D. Van Der Spoel, E. Lindahl, B. Hess, G. Groenhof, A. E. Mark, H. J. C. Berendsen, GROMACS: Fast, flexible, and free. *J. Comput. Chem.* **26**, 1701–1718 (2005).
36. T. Chen, N. Tsujimoto, E. Li, The PWWP domain of Dnmt3a and Dnmt3b is required for directing DNA methylation to the major satellite repeats at pericentric heterochromatin. *Mol. Cell. Biol.* **24**, 9048–9058 (2004).
37. L.-Y. Chen, Y.-C. Huang, S.-T. Huang, Y.-C. Hsieh, H.-H. Guan, N.-C. Chen, P. Chuankhayan, M. Yoshimura, M.-H. Tai, C.-J. Chen, Domain swapping and *SMYD1* interactions with the PWWP domain of human hepatomaderived growth factor. *Sci. Rep.* **8**, 287 (2018).

38. W. Tian, P. Yan, N. Xu, A. Chakravorty, R. Liefke, Q. Xi, Z. Wang, The HRP3 PWWP domain recognizes the minor groove of double-stranded DNA and recruits HRP3 to chromatin. *Nucleic Acids Res.* **47**, 5436–5448 (2019).
39. M. Zhang, M. Lei, S. Qin, A. Dong, A. Yang, Y. Li, P. Loppau, T. R. Hughes, J. Min, Y. Liu, Crystal structure of the BRPF2 PWWP domain in complex with DNA reveals a different binding mode than the HDGF family of PWWP domains. *Biochim. Biophys. Acta* **1864**, 194688 (2021).
40. N. Z. Lue, E. M. Garcia, K. C. Ngan, C. Lee, J. G. Doench, B. B. Liau, Base editor scanning charts the DNMT3A activity landscape. *Nat. Chem. Biol.* **19**, 176–186 (2022).
41. C.-C. Cho, C.-Y. Fei, B.-C. Jiang, W.-Z. Yang, H. S. Yuan, Molecular mechanisms for DNA methylation defects induced by ICF syndrome-linked mutations in DNMT3B. *Protein Sci.* **33**, e5131 (2024).
42. A. Micsonai, F. Wien, E. Bulyaki, J. Kun, E. Moussong, Y.-H. Lee, Y. Goto, M. Refregiers, J. Kardos, BeStSel: A web server for accurate protein secondary structure prediction and fold recognition from the circular dichroism spectra. *Nucleic Acids Res.* **46**, W315–W322 (2018).
43. K. Boyko, O. Arkova, A. Nikolaeva, V. O. Popov, P. Georgiev, A. Bonchuk, Structure of the DNMT3B ADD domain suggests the absence of a DNMT3A-like autoinhibitory mechanism. *Biochem. Biophys. Res. Commun.* **619**, 124–129 (2022).
44. J. Jumper, R. Evans, A. Pritzel, T. Green, M. Figurnov, O. Ronneberger, K. Tunyasuvunakool, R. Bates, A. Žídek, A. Potapenko, A. Bridgland, C. Meyer, S. A. A. Kohl, A. J. Ballard, A. Cowie, B. Romera-Paredes, S. Nikolov, R. Jain, J. Adler, T. Back, S. Petersen, D. Reiman, E. Clancy, M. Zielinski, M. Steinegger, M. Pacholska, T. Berghammer, S. Bodenstein, D. Silver, O. Vinyals, A. W. Senior, K. Kavukcuoglu, P. Kohli, D. Hassabis, Highly accurate protein structure prediction with AlphaFold. *Nature* **596**, 583–589 (2021).
45. W. L. Jorgensen, D. S. MaxwellJulian, J. Tirado-Rives, Tirado-Rives, Development and testing of the OPLS all-atom force field on conformational energetics and properties of organic liquids. *J. Am. Chem. Soc.* **118**, 11225–11236 (1996).

Acknowledgments: We thank the staff members of beamlines TLS23A1 and TPS25A for assistance in the SAXS experiments, as well as beamlines TLS15A and TPS05A for crystal diffraction data collection in the National Synchrotron Radiation Research Center, Hsin-Chu, Taiwan, ROC. We also acknowledge the Biophysics Core of the Institute of Molecular Biology for the fluorescence-based, circular dichroism, and mass analyses of the DNMT3B and 3L protein samples, as well as the Sequencing Core Facility (AS-CFII-111-211) in Academia Sinica. **Funding:** This work was supported by Academia Sinica postdoctoral fellowship (to C.-C.C.) and National Science and Technology Council MOST111-2311-B001-011-MY3 (to H.S.Y.). **Author contributions:** Conceptualization: C.-C.C. and H.S.Y. Methodology: C.-C.C., B.-C.J., H.-H.H., and W.-Z.Y. Investigation: C.-C.C., B.-C.J., and Y.-N.C. Supervision: C.-C.C. and H.S.Y. Writing: C.-C.C. and H.S.Y. **Competing interests:** The authors declare that they have no competing interests. **Data and materials availability:** Coordinates and structure factors for the PWWP domain from DNMT3B have been deposited in the PDB under accession code 8ZLK. SAXS data have been deposited in the SASBDB as entries SASDVZ8, SASDVK9, SASDVL9, SASDVM9, SASDV29, and SASDVJ9. All data needed to evaluate the conclusions in the paper are present in the paper and/or the Supplementary Materials.

Submitted 22 November 2024
Accepted 20 February 2025
Published 26 March 2025
10.1126/sciadv.adu8116